Dynamics of a new seismic isolation device based on tribological smooth rocking (TROCKSISD)

Maurizio Froli, Linda Giresini*, Francesco Laccone

Department of Energy, Systems, Territory and Construction Engineering, University of Pisa, Pisa (PI), Italy

Institute of Information Sciences and Technologies 'A. Faedo' National Research Council of Italy, Via G. Moruzzi 1, 56124 Pisa,

m.froli@ing.unipi.it, linda.giresini@unipi.it, francesco.laccone@isti.cnr.it-francesco.laccone@destec.unipi.it

*corresponding author.

Abstract

A novel isolation device is introduced to seismically protect slender structures or historic assets within the philosophy of Damage Avoidance Design (DAD). This device is conceived to allow smooth, controlled and damped rocking thanks to spherical contact surfaces, elastic springs which ensure re-centering, frictional layers and viscous elastic dampers able to dissipate energy during motion. The conceptual framework of the device is analyzed, and corresponding equations of motions obtained for the equivalent two degrees-of-freedom system. The proposed Performance Based Approach allows identifying geometric and mechanical features of the system. Extensive dynamic analyses with spectra-compatible ground motions are performed and the primary contribution of friction, developed by the relative slip of the two spherical surfaces, is discussed. Finally, the dynamic response under selected earthquakes is evaluated by comparing the isolated and the corresponding not isolated response, to highlight the beneficial effects produced by the proposed isolation technique.

Keywords

Damage Avoidance Design; rocking; seismic protection; seismic isolation; vibration control; friction

1. Introduction

A classical approach in earthquake engineering invokes the performance-based Capacity Design for which the formation of plastic hinges is necessary to dissipate energy provided by the ground motion. Despite human lives and goods are preserved with this approach, high and medium-high return period events cause damages not only on secondary components but also on primary structural members. Moreover, repair costs are usually as high as rebuilding costs and, in the immediate post-event time, the reconstruction can be unsafe and sometimes useless. Damage Avoidance Design (DAD) and other isolation techniques were therefore proposed as alternative design paradigms in earthquake engineering. DAD design philosophy was set out by Mander and Cheng [1] and later applied for practical cases of braced frame structures [2], among others. However, this concept was not completely new at that time, neither in the theoretical research nor into building practice. Following the early Housner's work [3], related to a non-smooth contact problem, efforts were spent on studying the rocking motion of rigid blocks; Meek [4] introduced the coupled effect of flexibility of the bracing with rocking of foundation, and Aslam et al. [5] the effect of pre-stressing. As for the rocking of rigid bodies, a control of rocking motion was recently proposed through a tuned pendulum, with analytical approach based on Lagrange formulation and Galerkin approximation method [6]. On the other hand, frictional problems were

treated in rigid block limit analysis of masonry structures [7], [8], based on specific formulations of 3D yield conditions for contact interfaces [9]. Friction sliding connections and rocking resisting systems may be found in ancient Greek and Roman temples or in Japanese Pagodas [10], and this is probably why some of these buildings survived so long, not sensitively damaged by earthquakes. More recent examples of DAD structures are the 315 m span South Rangitikei Bridge [11] and the 35 m high tower of Christchurch [12]. Other examples are the Alan Macdiarmid Building at Victoria University in Wellington and Southern Cross Endoscopy Building in Christchurch [13], both located in New Zealand. DAD structures follow the principles of isolation, with absence of damage and energy dissipation, and give the possibility of controlling displacements, to respect specific limit states. These characteristics are based on the rocking behavior, whose analytical framework was extensively investigated in the past. When discussing about rocking, it is necessary to distinguish between rigid contact problems - where the base of the rocking element can be considered rigid - and elastic contact models - where the base exhibits elasticity. For the first typology, rocking is able to describe the seismic behavior of rigid structural elements such as, for instance, masonry walls in out-of-plane modes. Diverse contributions were provided for analyzing the rocking response of walls in free configuration [14], [15] or for horizontally [16]–[19] or vertically [20] restrained walls. For masonry structures the assumption of rigid blocks is generally acceptable, but for other materials, several authors included the elasticity of the superstructure in the formulation [21]–[24]. In addition, the dynamics of an elastic structure coupled with a rocking wall was analyzed by [20]. In the context of elastic contact models, Psycharis and Jennings [25] firstly proposed the rocking rigid block on an elastic foundation realized through coupled springs and dampers. These models were recently used, properly updated, for new isolation techniques, for instance to protect marble structures [26], showing that these devices are highly performant to sustain seismic actions. However, still only few contributions are available to quantify the base isolation properties allowed by free rocking [27], [28], which is the core of the DAD philosophy. A novel semi-active on–off control strategy for the seismic protection of monolithic art objects is proposed in [29]. It consists in switching the stiffness of the anchorages located at the two base corners of the rocking block between two values. In this framework of elastic contact models, the present paper proposes an innovative device, conceived by M. Froli, able to protect from damages different types of superstructures by following the DAD principles. In general, the device allows a favorable dynamic behavior since:

(i)   in case of low-intensity excitation, the superstructure remains undamaged, so that the post-event serviceability is preserved;

(ii)   in case of a strong excitation, the motion of the superstructure is mitigated by a frictional contact and the effect of dampers, enabling the structure to smoothly rock.

The use of this device aims at limiting the damage of slender structures and valuable objects under seismic actions and vibrations. The acronym of this device has been inspired by its mechanics: TROCKSISD (Tribological ROCKing Seismic ISolation Device).

The art objects seismic risk mitigation is a systemic problem, in which it is crucial to understand in a first step the interdisciplinary and interrelated aspects of conservation, safety and exhibition requirements (especially geometric and aesthetic settings) [30], [31], [32]. Such devices can be effectively integrated as anti-seismic basement of highly vulnerable statues [33], [34]. Moreover, it is necessary to estimate the seismic behavior of the building where the object is located, and the effect of mechanical coupling in order to estimate the real seismic demand on the object to protect. Since the present study is focused on the dynamics of the TROCKSISD, for the sake of simplicity the ground seismic action is considered as input.

The concept and the equations of motion are obtained for the corresponding two degrees of freedom (2DOF) system (Section 2), whereas the main design steps are discussed in Section 3 to geometrically and mechanically design the device in a performance-based perspective. Afterwards, a quantitative estimation of the response of the system is obtained by performing nonlinear dynamic analyses (Section 4), and finally a parametric analysis is carried out to estimate the influence of friction on the global behavior of the dynamic system (Section 5).

2. Tribological ROCKing Seismic ISolation Device - TROCKSISD

2.1 Concept

The TROCKSISD consists of an articulated jointed connection to be installed between the foundation and the structure, which needs to be protected from earthquakes and vibrations, herein defined as superstructure. The latter is allowed to smoothly oscillate by rotation around the center of a spherical cup, which is allocated under its base plate. Such movement occurs on a concentric concave saddle-shaped spherical cup, where the surfaces are frictionally connected. Polar-symmetric viscous elastic dampers provide additional damping and stiffness to ensure re-centering capability. Two main phases can be identified in the response of the device: (i) a stick phase, where only the elasticity of the superstructure reacts to the external excitation, and smooth rocking is not activated, and (ii) a slip phase, where rocking is triggered and occurs over a frictional surface. A physical scaled mock-up of the device is shown in **Figure 1**: it is possible to observe the undeformed setting (**Figure 1**a), typical of the stick phase, and the deformed shape, representative of the slip phase (**Figure 1**b). In the mock-up, the viscous elastic dampers are realized as springs, to ease the re-centering effect.

The conception of the device is based on the necessity of enabling the jointed mechanism and controlling displacement demands, especially those generated by ground motion or vibrations of different nature. The friction is considered to prevent rocking of the superstructure at the SLS (Serviceability Limit State), as the jointed connection is behaving stiffly. On the other hand, at the ULS (Ultimate Limit State), the smooth rocking of the superstructure is admitted. This fixes an upper limit of the maximum rotation not to cause any damage of the components, i.e. due to accidental contact. The energy provided by the ground motion, due to earthquakes or other sources of vibration, has to be dissipated by TROCKSISD. This energy is dissipated by two systems working in parallel: one is friction at the interface level of substructure and superstructure, later illustrated in detail, and the other one consists of dampers located around the device edges (**Figure 1**). The amount of energy dissipated by the two systems depends on the values of frictional coefficient and on viscous damping coefficient. Moreover, this amount distributed into the two systems may be influenced by the motion type. As it will be explained in Section 5, it is necessary to control the two amounts of energy dissipated by dampers and frictional layer, as relevantly different behaviors occur at the variation of their characteristic parameters. The re-centering effect is not directly correlated to the frictional system, but only to the dampers, that are in parallel coupled with springs that recall the superstructure in an equilibrium position. The springs are in principle not pre-compressed, but a pre-compression would prevent, in case of vertical seismic shocks, detachment of the two spherical improving the seismic behavior.

| (a) | (b) |

Figure 1 TROCKSISD mock-up: (a) rocking prevented in stick phase, (b) rocking admitted in sliding phase.

Referring to **Figure 2**, the main components of the device and their functions are summarized in the following.

- The top plate (A in **Figure 2**) is a ribbed plate whose upper flat face allows the connection with the superstructure;
- The convex shaped spherical cup (B in **Figure 2**) plays multiple function of transmitting vertical and horizontal loading to the foundation, allowing the rotation of the jointed mechanism. Through its surface it allows energy dissipation by friction on the underlying concave saddle-shaped spherical plate. The spherical cup is centered in O and has radius of curvature R. The angle $\overline{\varphi}$ represents the latitude from the equator of the plane that cuts off the ideal sphere from which the surface is derived.
- The concave saddle-shaped spherical plate (C in **Figure 2**) is made of a curved steel plate installed on a ribbed plate, which is connected to the ground. This component is geometrically described by the angle φ_0 (complementary to the zenith angle), which identifies the latitude of the cut-off plane.
- Viscous-elastic dampers are conceived to link the perimeter of the upper plate and the concave shaped spherical plate, and to provide stiffness (k), damping (c), and re-centering capacity to the system. Dampers that result polar-arrayed are in even are installed in pairs, so that the elements of a group are positioned as opposing V bracing to help the system to self-center and to oppose torsional effects.

An axonometric view of TROCKSISD is shown in **Figure 3**a and an exploded three-dimensional view is in **Figure 3**b.
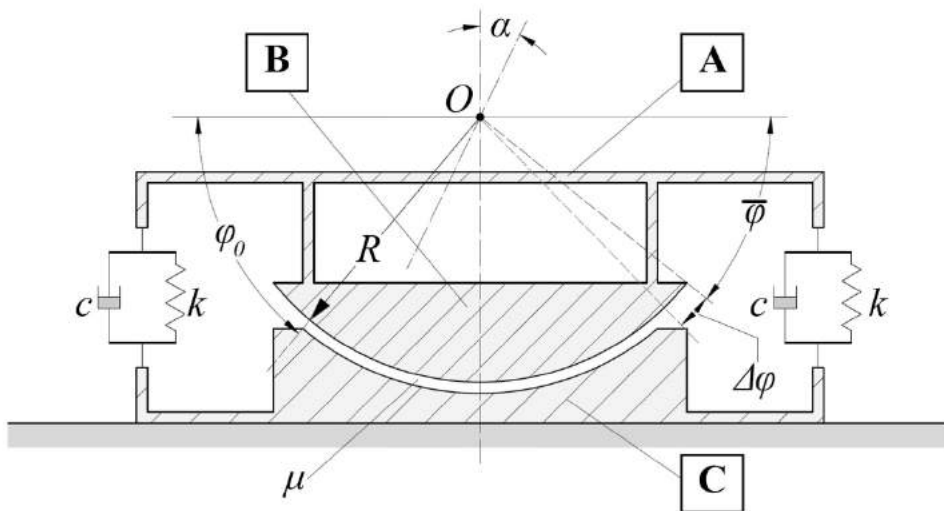
Figure 2 TROCKSISD: geometric and mechanical features in a schematic section view.
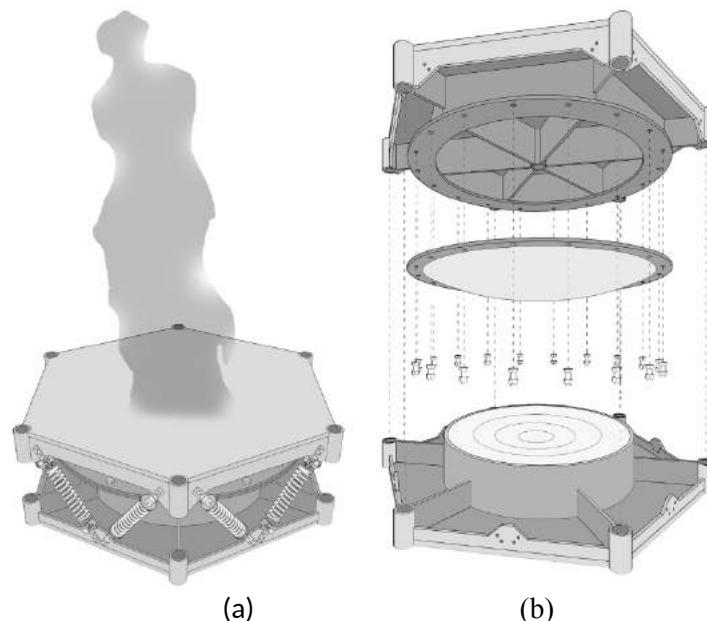
(a)   (b)
Figure 3 TROCKSISD: (a) axonometric view; (b) exploded view.

2.2 Analytical model

This paragraph describes the mechanics of TROCKSISD, in particular the estimation of the tribological moment developed between the convex spherical cup and the concave plate associated to the Coulomb friction model [35], and the equations of motion of the corresponding 2 DOFs system.

2.2.1 Modeling of friction forces

Coulomb friction model and evaluation of surface pressure

The Coulomb model [35] is adopted for the evaluation of friction: the problem is inherently nonlinear since the cases of static friction, where the reactive force prevents any movement, and dynamic friction, where the stick force is overcome and the body starts to slide, should be distinguished.

The contact pressures at the interface of the two sliding surfaces (B and C of **Figure 2**) can be approximately evaluated as follows. Let R be the radius of the surface, and φ_0 the complementary to the zenith angle; the concentric spherical cups are supposed rigid and mutually connected by radial compression-only uniformly-distributed springs of stiffness k_p, which are representative of the surface pressure. Two load cases of vertical (P) and horizontal (H) loading are evaluated separately, and, because of the linearity of the problem, their effects in terms of spring compression or de-compression are then be superimposed. A polar coordinate system (R, θ, φ) is adopted, where R and φ have the meaning of radial and zenithal components, while θ stands for the azimuthal angle (**Figure 2**).
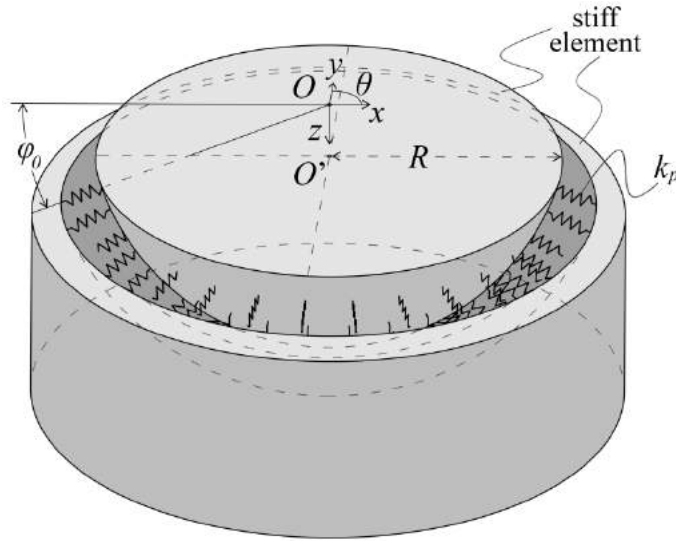
Figure 4 Scheme adopted for the evaluation of contact pressures.

Under vertical loading P, the problem is polar symmetric with respect to the z axis (**Figure 5**). The radial stress for simple monodimensional spring elements can be expressed with the Hooke's law, where the term k_p in Eq. (1) refers to the stiffness of the compression-only uniformly-distributed springs (**Figure 2**):

$$\sigma_r(\varphi) = k_p v_z \sin(\varphi) \tag{1}$$

dp_r displayed in Figure 5a is the infinitesimal pressure in radial direction, equal to:

$$dp_r = \sigma_r dA = \sigma_r(\varphi) \, R^2 \cos(\varphi) \, d\varphi \, d\theta \tag{2}$$

However, due to the geometry of load it is convenient to extrapolate from the previous equation the dp_r vertical component dp_z:

$$dp_z = dp_r sin(\varphi) = k_p v_z R^2 cos(\varphi) \ sin^2(\varphi) \ d\varphi \ d\theta \qquad (3)$$

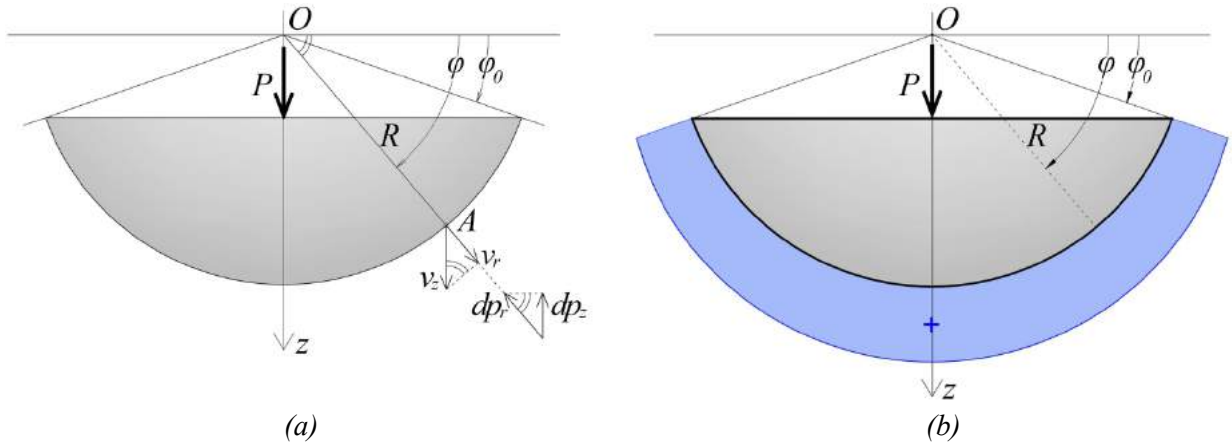The vertical displacement v_z is obtained by equilibrium.

$$P = k_p v_z R^2 \int_0^{2\pi} \int_{\varphi_0}^{\pi/2} cos(\varphi) sin^2(\varphi) d\varphi d\theta$$

$$v_z = \frac{3P}{2\pi k_p R^2 [1 - sin^3(\varphi_0)]} \qquad (4)$$

Substituting Eq. (4) in Eq. (1) yields the pressure $\sigma_r^P(\varphi)$ due to vertical load.

$$\sigma_r^P(\varphi) = \frac{3 \ P}{2\pi R^2} \frac{sin(\varphi)}{1 - sin^3(\varphi_0)} \qquad (5)$$

Because of the symmetry of the problem, $\sigma_r^P(\varphi)$ is independent from the coordinate θ. A qualitative profile of the compressive pressure is shown in **Figure 5**b.
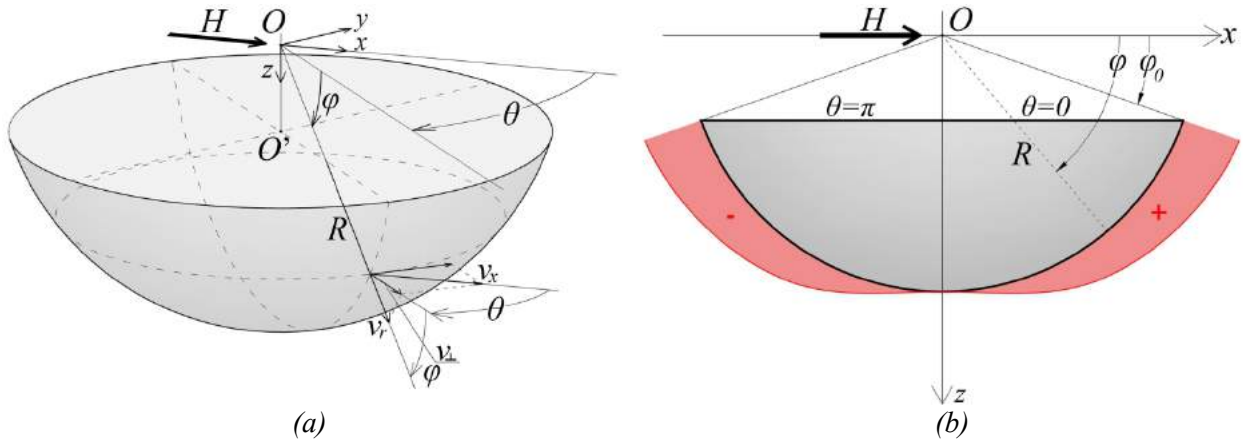

(a)   *(b)*

Figure 5 Evaluation of surface pressure due to vertical loading P: displacement parameters (a) and schematic contact pressures (Eq. **Error! Reference source not found.**) (b).

The base shear force of the superstructure H acting on the curvature center O (**Figure 6**) is transferred as horizontal loading on the device. The pressure is dependent on both the angular components, and its qualitative plot is antisymmetric with respect to the plane yz. Adopting the previous methodology based on an equilibrium condition, the horizontal displacement v_x is equal to (**Figure 6**a):

$$v_x = \frac{12 \ H}{\pi k R^2 [8 - 9sin(\varphi_0) - sin(3\varphi_0)]} \qquad (6)$$

whereas the pressure $\sigma_r^H(\varphi,\theta)$ (positive or negative depending on the sign of H has this form (**Figure 6**b):

$$\sigma_r^H(\varphi,\theta) = \frac{12 \ H}{\pi R^2 [8 - 9sin(\varphi_0) - sin(3\varphi_0)]} cos(\theta) cos(\varphi) \qquad (7)$$

(a)   *(b)*

Figure 6 Evaluation of surface pressure due to horizontal loading H: displacement parameters (a) and schematic contact pressures (b).

Since the elastic radial springs are supposed monolateral, the negative pressure in **Figure 6**b should be regarded as a de-compressive action with respect to the compressive values obtained from the vertical loading P. The superposition of the effects (**Figure 7**a) yields:

$$\sigma_r(\varphi,\theta) = \sigma_r^P(\varphi) + \sigma_r^H(\varphi,\theta) \tag{8}$$

(a)   (b)
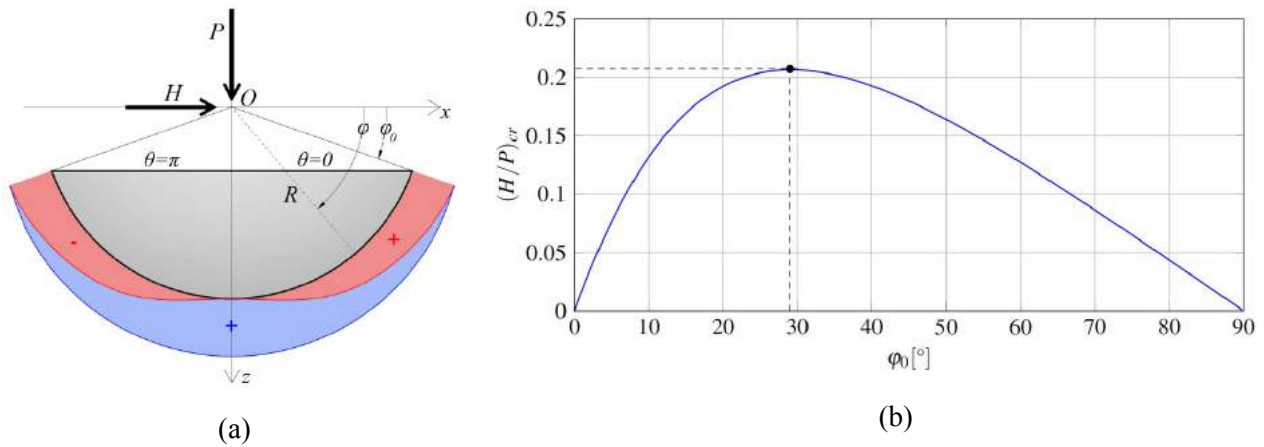
Figure 7 Superposition of the surface pressures deriving from vertical loading (blue) and horizontal loading (red) (a); critical base shear to vertical load ratio depending on the geometry parameter (b).

Once the surface pressure is known, it is possible to use the obtained stress value for a preliminary verification of strength. The de-compressing condition is defined when the total pressure (Eq. (8)) is locally null. This at least occurs at $\varphi = \varphi_0$ and $\theta = \pi$:

$$\sigma_r^P(\varphi_0) + \sigma_r^H(\varphi_0,\pi) = 0 \tag{9}$$

That is, substituting in Eq. (9) Eqs. (5)**Error! Reference source not found.** and (7):

$$\frac{3\,P}{2\pi R^2}\frac{sin(\varphi_0)}{1 - sin^3(\varphi_0)} - \frac{12\,H}{\pi R^2[8 - 9sin(\varphi_0) - sin(3\varphi_0)]}cos\,(\varphi_0) = 0 \tag{10}$$

This equations gives, properly modified, the critical ratio $\left(\frac{H}{P}\right)_{cr}$ of horizontal and vertical forces:

$$\left(\frac{H}{P}\right)_{cr} = \frac{8 - 9\sin(\varphi_0) - \sin(3\varphi_0)}{8\left[1 - \sin^3(\varphi_0)\right]} ta \qquad (11)$$

which is function of the only geometrical design parameter φ_0. The selection of φ_0 may reasonably lead to a value within the boundary drawn by the $(H/P)_{cr}$ curve of **Figure 7**b in order to maximize the frictional dissipative contribution and avoid decompression. The maximum of the curve is around $\varphi_0 = 30°$ with the ratio $H/P = 0.2$.

Tribological moment

The desired rocking of the superstructure essentially causes frictional sliding. Being friction a reactive force, its contribution may be expressed in the analytical formulation of the problem by means of the tribological moment M_μ. It is possible to assume as simplifying hypotheses that:

i.   if we consider a small rocking rotation around a generic axis t-t, the trajectory of a generic point A on the spherical surface is an arc of circle, obtainable by intersection of the spherical cup surface with a plane through the point A whose normal is parallel to the t-t axis (**Figure 8**);

ii. the radial pressure (Eq. (8)) is constant during motion;

iii. the effect of horizontal force acting on the device is antisymmetric, so its contribution is globally null if the decompression condition is not overcome. Thus, only pressure generated by vertical loading is considered;

iv. the tangential friction component is locally orthogonal to the radial pressure, and oriented in the direction of the tangent to the circular trajectory found as per the first point.

Condition (ii) is assumed valid as the extension of the contact surfaces are constant over motion. This is guaranteed by a proper design of the spherical cup, where the angular sliding stroke $\Delta\varphi$ is greater than a fixed limit (**Figure 2**). The response of the device takes into account this design parameter (for more details the reader is referred to Section 4).

The tangential fiction component may be expressed as:

$$\tau = \mu\sigma_r \qquad (12)$$

In infinitesimal terms, it holds:

$$d\tau = \mu \, dp_r \qquad (13)$$

where $dp_r = \sigma_r^P(\varphi) \, dA$ is the infinitesimal radial pressure (**Figure 8**b), namely the radial pressure due to vertical loading $\sigma_r^P(\varphi)$ over the infinitesimal area $dA = R^2\cos\varphi d\varphi d\theta$. In a generic point of the surface, the contribution of friction can be expressed as the infinitesimal tribological moment dM_μ (Eq.(14)), multiplying the tangential resistance $d\tau$ to the lever arm $b(R,\theta,\varphi)$:

$$dM_\mu = b(R,\theta,\varphi) \, d\tau \qquad (14)$$

where:

$$b(R,\theta,\varphi) = R\sqrt{\sin^2(\varphi) + \cos^2(\varphi)\sin^2(\theta)} \qquad (15)$$

Substituting Eqs. **Error! Reference source not found.**, (12) and (15) into Eq. (14) and integrating, the tribological moment M_μ assumes the form:

$$M_\mu = \frac{3\mu PR}{2\pi\left(1 - \sin^3(\varphi_0)\right)} \int_0^{2\pi} \int_{\varphi_0}^{\frac{\pi}{2}} \sin(\varphi)\cos(\varphi)\sqrt{\sin^2(\varphi) + \cos^2(\varphi)\sin^2(\theta)}\, d\varphi\, d\theta \qquad (16)$$
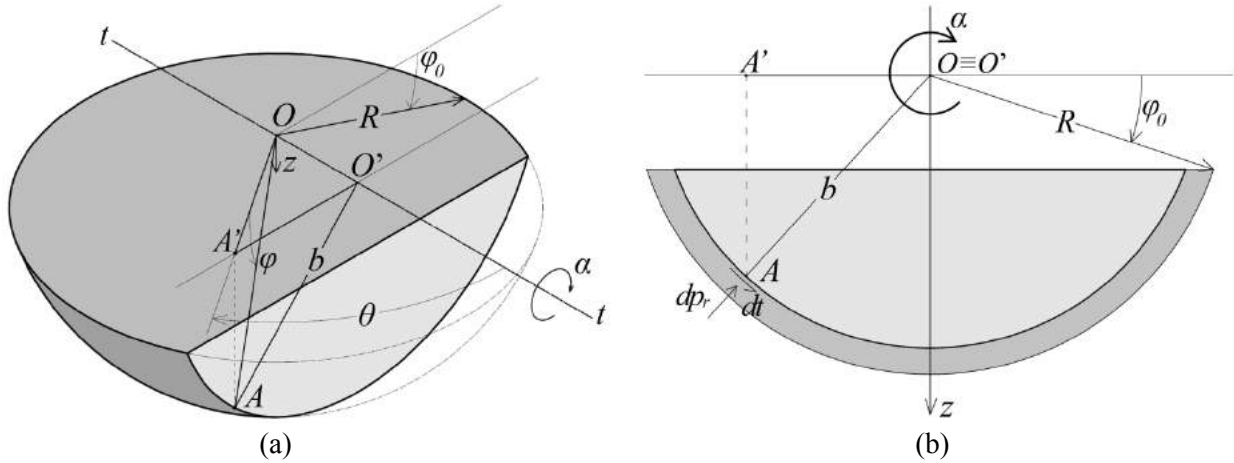
The expression clearly identifies a dependency on two geometric parameters, φ and R, which can be isolated in a more compact equation:
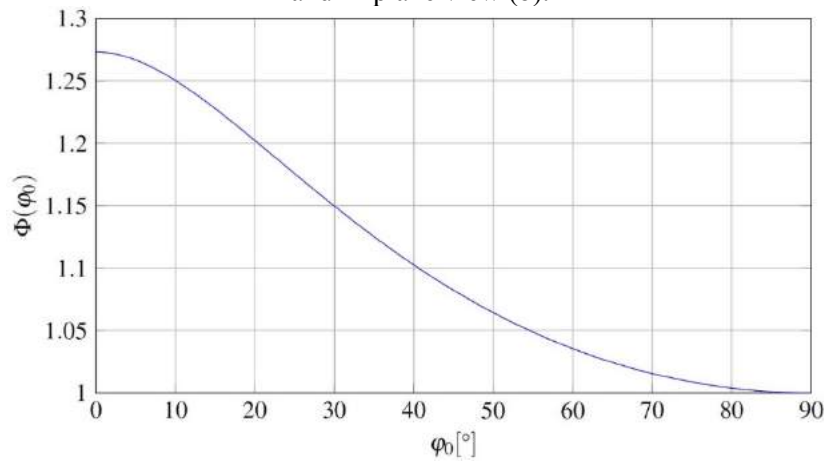
$$M_\mu = \mu PR\Phi(\varphi_0) \qquad (17)$$

where $\Phi(\varphi_0)$ is a function of the only polar coordinate φ_0:

$$\Phi(\varphi_0) = \frac{3}{2\pi\left(1 - \sin^3(\varphi_0)\right)} \int_0^{2\pi} \int_{\varphi_0}^{\frac{\pi}{2}} \sin(\varphi)\cos(\varphi)\sqrt{\sin^2(\varphi) + \cos^2(\varphi)\sin^2(\theta)}\, d\varphi\, d\theta \qquad (18)$$

that has values between $\Phi(0°) = 1.273$ and $\Phi(90°) = 1$, and whose trend curve is represented in **Figure 9**.

(a)   (b)

Figure 8 Scheme of the geometrical parameters involved in the tribological moment formulation: 3D (a) and in-plane view (b).

Figure 9 Variable function $\Phi(\varphi_0)$ affecting the tribological moment (Eq. (18)).

2.2.2 Proposed 2DOF model

The dynamics TROCKSISD is here analytically formulated. For the polar-symmetry of the system, the response is assumed to be independent from the direction of the seismic excitation; therefore, a schematic plan representation of the problem as in **Figure 10**a is assumed to be representative. Hence, the superstructure that

is rigidly connected to the top plate of the jointed device is regarded as a SDOF oscillator. The dynamic behavior is described through the 2DOF model illustrated in **Figure 10**b. The dynamic parameters are all considered lumped.

The first DOF is representative of the superstructure and is described by the translational Lagrangian parameter x. The superstructure lumped mass m has distance h from the pivot point O, which is the center of the curvature of the jointed device. The superstructure has stiffness k and damping c.

The second DOF is described by the rotational Lagrangian parameter α. The mass of TROCKSISD m_b is located at the scheme point G_b, center of mass of the device, distant h_b from the pivot O. Being related with a rotational DOF, the characteristics of the dampers are expressed in terms of rotational stiffness and damping, k_φ and c_φ respectively. P-Delta effects should be also in principle considered in case of flexible springs. However, the following analysis holds for springs stiff enough to make the P-Delta effects negligible.

Figure 10 Representations of the system analyzed: (a) schematic view; (b) 2DOF model.

Referring to the free body diagram of forces of **Figure 11**, the equation of motion can be written as:

$$m\ddot{x} + c(\dot{x} - h\dot{\alpha}) + k(x - h\alpha) = -m\ddot{x}_g \qquad (19)$$

or:

$$m_b h_b (\ddot{x}_b + \ddot{x}_g) + c_\varphi \dot{\alpha} + k_\varphi \alpha + M_\mu = -kh(x - h\alpha) - ch(\dot{x} - h\dot{\alpha}) \qquad (20)$$

where Eq. (19) concerns the first translational parameter x (top of **Figure 11**), whereas Eq. (20) is the rotational dynamic equilibrium around the pivot O (bottom of **Figure 11**). It can be noted that:

$$x_b = \alpha h_b \qquad (21)$$

where x_b is the horizontal displacement of G_b, approximately expressed in terms of the Larangian parameter α. Consequently, deriving two times:

$$\ddot{x}_b = \ddot{\alpha}\, h_b \qquad (22)$$

If eq.(22) is included in eq. (20), the following Eq. (23) can be obtained.

$$m_b h_b^2\, \ddot{\alpha} + \left(c_\varphi + ch^2\right)\dot{\alpha} + \left(k_\varphi + kh^2\right)\alpha - ch\dot{x} - khx + M_\mu = -\,m_b h_b \ddot{x}_g \qquad (23)$$

From which it is possible to recognize the moment of inertia $I_b = m_b h_b^2$ with respect to the pivot O. If the dynamic loadings are written as Eq. (24), the equation of motion can be rewritten as Eq. (25).

$$\begin{cases} \overline{F} = -\, m\ddot{x}_g \\ \overline{M} = -\, m_b h_b \ddot{x}_g \end{cases} \qquad (24)$$

and therefore:

$$\begin{cases} m\ddot{x} + c\dot{x} - ch\dot{\alpha} + kx - kh\alpha = \overline{F} \\ I_b\ddot{\alpha} + \left(c_\varphi + ch^2\right)\dot{\alpha} + \left(k_\varphi + kh^2\right)\alpha - ch\dot{x} - khx + M_\mu = \overline{M} \end{cases} \qquad (25)$$
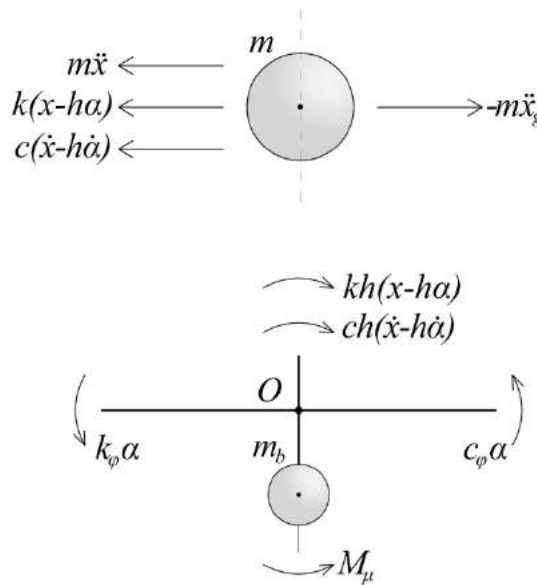
Figure 11 Free body diagram of forces for the 2DOFs.

The dynamic motion obtainable from this formulation, as any problem dealing with friction contact, may show the following three phases.

- In the **static phase**, at a given time the velocity equals zero, i.e. angular acceleration $\ddot{\alpha} = 0$, so there is absence of motion. The causes could be either the absence of excitation or a break of the mass. In the latter, even in a deformed position of the mass, the block continues to be stuck unless the elastic force or the dynamic loading is greater than the static friction force.
- The **incipient motion phase** is the condition in which the velocity is still zero, but the static friction force is overcome. Thereafter, accelerations and inertial forces develop because of the variation of velocity.
- The **dynamic phase** is characterized by a non-zero velocity; the dynamic friction force has the sign of the velocity to describe the opposition to the direction of motion.

As a consequence, a pure stick behavior is obtained if there is static phase over the monitoring time. A pure slip motion expresses vice versa the conditions for the dynamic phase. A mixed slip-stick motion manifests both phases with incipient motions included. To embrace all the phases of motion in a single mathematical

formulation, the system is solved via numerical integration with the Euler-Gauss method [36] into time domain of the equations reorganized as:

$$\begin{cases} \ddot{x} = \dfrac{\overline{F}}{m} + \dfrac{c}{m}\dot{x} - \dfrac{ch}{m}\dot{\alpha} + \dfrac{k}{m}x - \dfrac{kh}{m}\alpha \\[2mm] \ddot{\alpha} = \dfrac{1}{I_b}\left[\overline{M} - \left(c_\varphi + ch^2\right)\dot{\alpha} - \left(k_\varphi + kh^2\right)\alpha + ch\dot{x} + khx - M_\mu\right] \end{cases} \tag{26}$$

The initial conditions expressing the system stillness are imposed to be:

$$\begin{cases} x_1 = x(0) = 0 \\ \dot{x}_1 = \dot{x}(0) = 0 \\ \alpha_1 = \alpha(0) = 0 \\ \dot{\alpha}_1 = \dot{\alpha}(0) = 0 \end{cases} \tag{27}$$

A tolerance is added to define a stick region in the neighborhood of null velocity $\dot{\alpha} = 0$.

2.3 Materials

The characteristics of materials employable in the TROCKSISD are fundamental not only to define the strength and stiffness of the components, but also to determine the friction coefficient between the sliding surfaces. Common steel can be used for all the components, while for the sliding surfaces also stainless steel and anodized aluminum may be used. To achieve a lower friction coefficient, the concave spherical cup may be covered with PTFE. In the analytical model the friction coefficient is assumed to be constant.

3. Design criteria

The design of TROCKSISD requires the selection of both geometrical and mechanical parameters on the basis of the desired performances. The proposed approach for sizing the components aims at achieving target rotations corresponding to certain level of actions, defined in the Eurocodes as Limit States. It seemed reasonable set zero value rotations at the SLS and to design the jointed mechanism to stick. Hence, the level of seismic forces is tolerable, and superstructure is designed to react elastically, therefore, there is no need for isolation. Imposing the static phase, residual rotations that the presence of friction as a nonlinear action may cause are avoided.

Smooth rocking of the superstructure and energy dissipation occur at ULS during the slip motion of the device. However, at this level neither the dampers stroke shall attain the maximum extension limit nor any other part of the device shall fail because of accidental crashes due to mutual contact. The superstructure results isolated and can still elastically behave without damaging.

3.1 Geometry design

In stick motion the system behaves as a SDOF oscillator; such a behavior is foreseen at the Serviceability Limit State. The unique inertial force is applied at the superstructure mass m. Its maximum value occurs for the maximum acceleration $\ddot{x}_{max}$, when contemporarily the displacement is maximum x_{max} and the velocity is null $\dot{x} = 0$ (**Figure 12**). Moreover, the mass m_b motion is integral with the ground motion, so the PGA value can be assumed as acceleration. The inequality is imposed as a design condition.

$$M_{Ed} \leq M_{\mu,s} \tag{28}$$

The two terms in Eq. (28) represent respectively the SLS design moment M_{Ed} (Eq.(29)) and the tribological static moment $M_{\mu,s}$ (Eq.(30)) descending from Eq. (17).

$$M_{Ed} = mh\ddot{x}_{max} - m_b h_b PGA \tag{29}$$

$$\text{M}_{\mu,s} = \mu_s PR\Phi(\varphi_0) \tag{30}$$

Which substituting in Eq. (28) yield:

$$m\, h\, a_{g,max} - m_b h_b PGA \leq \mu_s PR\Phi(\varphi_0) \tag{31}$$

By algebraically modifying the inequality, Eq. (32) yields the condition for the minimum radius compatible with the desired SLS behavior, once a value of φ is selected preliminarily.

$$R_{min} \geq \frac{ma_{g,max}[H + \Delta h] - m_b PGA[y_G - \Delta h]}{\mu_s P\Phi(\varphi_0) + sin(\overline{\varphi})[ma_{g,max} + m_b PGA]} \tag{32}$$

The radius can be found iteratively, updating the m_b value at each step. The value of Δh, height of the superstructure base plane from the cut plane of the cup, is to be selected based on the available amount of space at the base of the structure and feasibility requirements. $\Delta\varphi$ is an angular sliding stroke that guarantees continuous friction development over a constant area during the motion (**Figure 13**).

$$R_{min} \geq \frac{ma_{g,max}[H + \Delta h] - m_b PGA[y_G - \Delta h]}{\mu_s P\Phi(\varphi_0) + sin(\overline{\varphi})[ma_{g,max} + m_b PGA]} \tag{33}$$

An idea of the maximum size the device occupies can be given by the parameter $\overline{D}$ (**Figure 13**) in the horizontal direction, which can be also be expressed in terms R_{min} as in Eq. (34). Moreover, while in the design phase, the mass $m_b = m_{b1} + m_{b2} + m_{b3}$ should be updated iteratively.

$$\overline{D}_{min} \geq 2R_{min}cos(\overline{\varphi}) \tag{34}$$
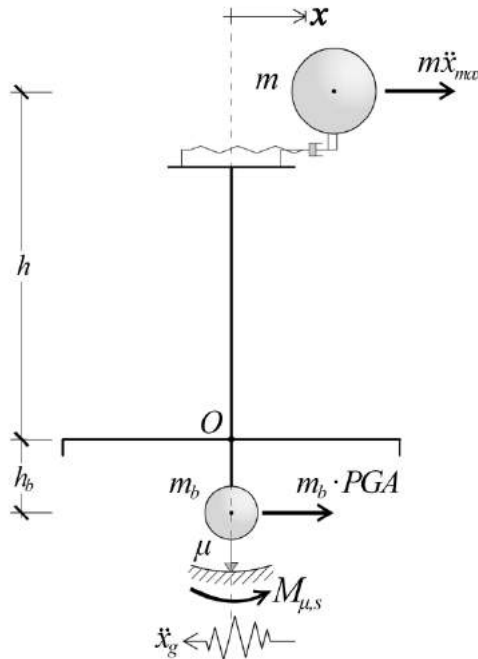
Figure 12 Design condition at SLS.
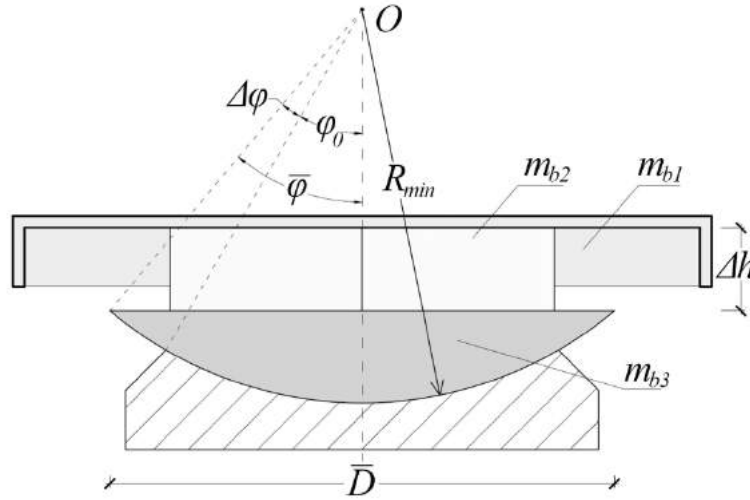
Figure 13 Geometric parameters to be defined in the design of TROCKSISD.

3.2 Calibration procedure for the identification of stiffness and damping parameters

At the ULS the design limitation can be expressed in terms of maximum rotation α. However, the rotations are influenced by friction developed at the sliding interface and viscous-elasticity of dampers. While the friction reaction is a constant and known value because the device has been geometrically defined at the SLS, the only variables to be determined at the ULS are the mechanical parameters k_φ and c_φ. Because the superstructure will result isolated at the ULS, it is suggested firstly to define a desired response in terms of vibration period, and then, to investigate a range of values of k_φ and c_φ, which combined permit to reach the rotation limitations. Therefore, a modal analysis of the system is required as first step. Then, once defined a design dynamic action, the characteristics of the dampers can be selected. If needed, the design procedure could be reiterated from the considerations at SLS.

3.2.1 Modal analysis

The equations of motion of the 2DOF system in case of free vibrations can be written as Eq.(35), or in matrix form as Eq. (36) (compact form Eq.(37)), not considering neither external dynamic loadings nor friction.

$$\begin{cases} m\ddot{x} + c\dot{x} - ch\dot{\alpha} + kx - kh\alpha = 0 \\ I_b\ddot{\alpha} + (c_\varphi + ch^2)\dot{\alpha} + (k_\varphi + kh^2)\alpha - ch\dot{x} - khx = 0 \end{cases} \tag{35}$$

$$\begin{bmatrix} m & 0 \\ 0 & I_b \end{bmatrix}\begin{Bmatrix} \ddot{x} \\ \ddot{\alpha} \end{Bmatrix} + \begin{bmatrix} c & -ch \\ -ch & c_\varphi + ch^2 \end{bmatrix}\begin{Bmatrix} \dot{x} \\ \dot{\alpha} \end{Bmatrix} + \begin{bmatrix} k & -kh \\ -kh & k_\varphi + kh^2 \end{bmatrix}\begin{Bmatrix} x \\ \alpha \end{Bmatrix} = \begin{Bmatrix} 0 \\ 0 \end{Bmatrix} \tag{36}$$

$$[M]\ddot{A} + [C]\dot{A} + [K]A = 0 \tag{37}$$

A simple modal analysis for an equivalent 2DOF system can be performed to dynamically characterize it, obtaining natural frequencies, modal shapes and associated masses [36].

4. Dynamic analysis, design application and comparison of the response with SDOF oscillator

An ideal case study is selected and analyzed to obtain quantitative information on the dynamic of the system. Seismic loading is expressed by means of response spectrum compatible accelerograms obtained from the site specifications. Consequently, the device is sized with the proposed performance-based approach. The results of the analysis are here presented and discussed in general terms.

4.1 Definition of the design case and seismic inputs

The dynamic loading, as defined in the analytical 2DOF model, is applied through a story of base ground accelerations $\ddot{x}_g$. Natural response spectrum compatible accelerograms (Table 1) are generated by the software REXEL v3.5 [37] on the basis of two target spectra, one for the SLS and one for the ULS. Seven accelerograms that provide a mean spectrum close to the code design response spectrum (within the upper limit of +30% and lower limit of -10%) are selected for both cases. As design case, the superstructure is supposed to have the features included in **Table 1**.

Table 1 Characteristics of the superstructure.

Parameter	Symbol (unit)	Value/Type
Mass	m (kg)	1500
Height of center of mass	h (m)	3.50
Fundamental vibration frequency	f_{ref} (Hz)	2.804
Fundamental vibration period	T_{ref} (s)	0.357
Stiffness	k (kN/m)	466
Damping ratio	ξ	0.01
Design working life category		4
Location		Castelnuovo di Garfagnana, Italy
Coordinates		44°07′19″N 10°24′20″E
Site class		B
Max pseudo-acceleration	$a_{g,max}$ (m/s^2)	2.27
Peak Ground Acceleration	PGA (m/s^2)	0.93

Accelerograms of **Table 2** are selected and scaled according to site and superstructure specification. Each of them is limited on a duration of 30 s. The characteristics of TROCKSISD are initially assumed as per **Table 3**, where the parameters are assumed by traditional experimental values. For more exact results, for instance referring to dynamic and static friction coefficients, some innovative experimental techniques are presented in [38]].

**Table 2** Selected ULS and SLS natural response spectra compatible accelerograms.

Accelerograms	Earthquake name	Date	Mw	PGA [m/s^2]	Accelerograms	Earthquake name	Date	Mw	PGA
S1 - ULS	Gazli	17/05/76	6.7	6.038	S1 - SLS	Friuli (aftershock)	15/09/76	6	2.136
S2 - ULS	Bucharest	04/03/77	7.5	1.690	S2 - SLS	Montenegro	-	6.9	2.361
S3 - ULS	Vrancea	30/05/90	6.9	0.373	S3 - SLS	Campano Lucano	23/11/80	6.9	1.526
S4 - ULS	Umbria Marche	26/09/97	6	0.185	S4 - SLS	Umbria Marche	26/09/97	6	5.138
S5 - ULS	Izmit	17/08/99	7.6	2.580	S5 - SLS	Umbria Marche	26/09/97	6	0.897
S6 - ULS	Izmit (aftershock)	13/09/99	5.8	0.3906	S6 - SLS	South Iceland	17/06/00	6.5	2.038
S7 - ULS	Izmit (aftershock)	13/09/99	5.8	0.3258	S7 - SLS	South Iceland	17/06/00	6.5	4.678
Mean			6.6	3.436	Mean			6.4	2.682

Table 3 Input characteristics of the TROCKSISD.

Parameter	Symbol (unit)	Value/Type
Mass of the device (approximated)	m_b (kg)	600
Height of the upper plate	Δh (m)	0.255
Angular sliding stroke	$\Delta\varphi$ (°)	5
Static friction coefficient	μ_s	0.18
Dynamic friction coefficient	μ_d	0.09

4.2 Design at SLS

The vertical loading, from which the tribological moment (Section 2) is derived, is obtained from the total mass of the system that is $m + m_b = 2100$ kg. To limit the dimension of the TROCKSISD, an upper limit of the diameter of the spherical cup base circle may be imposed. In the present case such value is arbitrarily selected to be $D_{max} = 1300$mm. The best value for the angle that can be found by plotting parametrically Eq.(34) (**Figure 14**) is $\varphi_0 = 72°$.
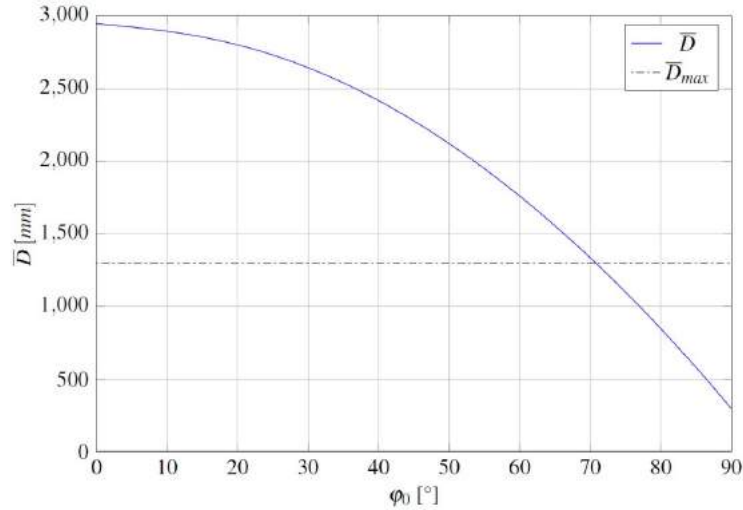
Figure 14 Case study design of the TROCKSISD at SLS.

Therefore, it can be consequently obtained:

$$\overline{\varphi} = \varphi_0 - \Delta\varphi = 67° \; ; \; R = 1664 \text{ mm} \tag{38}$$

To be on the safe side the final value $R = 1685$ mm is adopted. Based on the radius value found R, the following variables can be updated:

$$h = 2.204 \text{ m} \; ; \; m_b = 1019 \text{ kg} \tag{39}$$

4.3 Modal analysis and design at ULS

The eigenvalue problem solved parametrically by varying the rotational stiffness k_α yields the periods represented in **Figure 15**a. It can be observed that for higher values k_α, the second period T_2 tend towards zero, while contemporarily the first period T_1 asymptotically approaches the value of T_{ref} (dash-dot line in **Figure 15**a), which is the period of the superstructure considered as SDOF. This result confirms the accuracy of the analytical model because the larger is the stiffness, the closer to a rigidly connected basement results TROCKSISD.
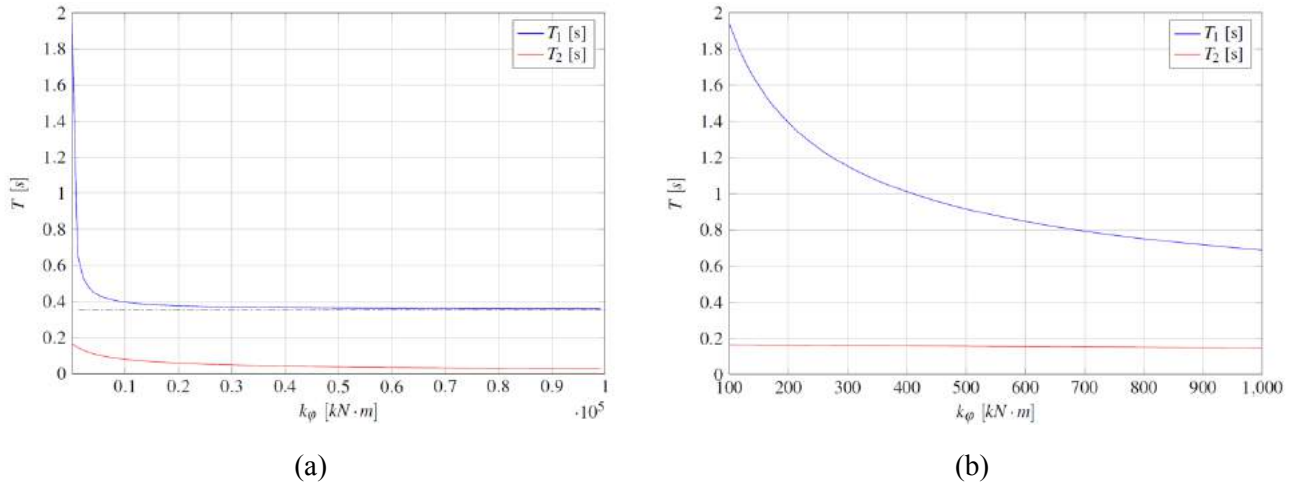
Rescaling **Figure 15**a, the variables are plotted in **Figure 15**b in a more interesting k_α range of values ($100 - 1000$ kN m). Hence, the first period T_1 is within the values of more than 0.6 s and less than 2.0 s. This guarantees a high isolation level for the superstructure that otherwise would have been submitted to the maximum acceleration level (at the *plateau* of the response spectra for $T_{ref} = 0.357$s). In the same range, T_2 is approximately constant. The optimal value of T_1, and similarly of k_α, is such that the seismic loading is lowered but the displacement demand can still be met by the components.

In the $k_\alpha$range of interest, the modal mass associated with the first mode of vibration M_1 is clearly prevalent with respect to M_2 and represents about the 90% of the dynamic mass of the system. Assuming e.g. $k_\alpha = 500$kNm, the following modal shapes are obtained:
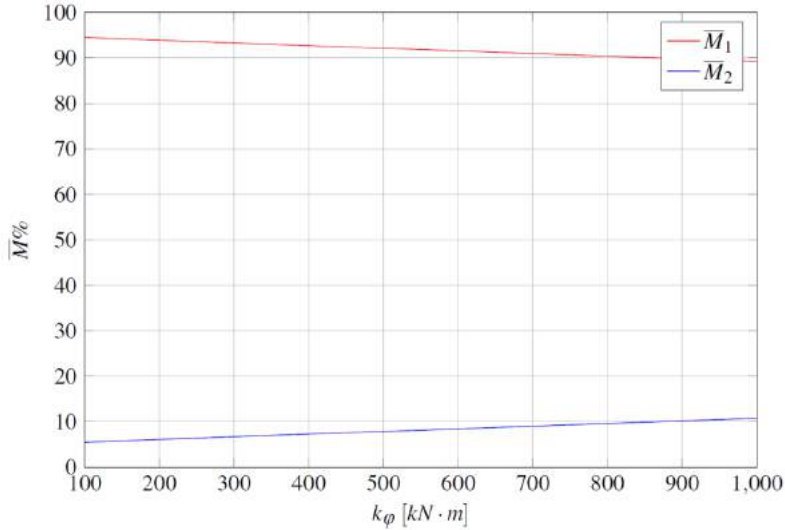
$$\{\Phi_1\} = \left\{ \begin{array}{c} -0.0239 \\ -0.0089 \end{array} \right\}; \{\Phi_2\} = \left\{ \begin{array}{c} +0.0097 \\ -0.0219 \end{array} \right\}, \tag{40}$$

displayed in **Figure 16**-Figure 17.

(a)   (b)

Figure 15 Periods of vibration T_1 and T_2 in the range of $k_\varphi = 0 - 100000$ kNm (a) and of $k_\varphi = 100 - 1000$ kNm (b).


**Figure 16** Modal masses M1 and M2 in the range of $k_\varphi = 100$-1000 kN m.

The optimal values of both mechanical parameters k_φ and c_φ can be found from the displacement spectra of the second Langrangian parameter α, obtained by solving the numerical problem (Eq.(24)) with the (seven) selected seismic records. Parametrically varying the stiffness k_φ, the superstructure presents different periods. At each step in the period range of interest ($T_1 = 0.7 - 1.9$s, **Figure 15**b), two significant values from the rotation time-history are considered:

- their absolute maximum α_{max}, selected among the maximum absolute rotation values of all the seismic records (and therefore referred to an individual acceleration time-history);
- their mean value $\overline{\alpha_{max}}$: the maximum absolute rotation value is selected for each acceleration time-history, and from these seven values the mean value is derived.

These values are plotted respectively in **Figure 18**a, obtaining a classic displacement spectrum of α_{max}, and **Figure 18**b, a displacement spectrum of mean values $\overline{\alpha_{max}}$. In these graphs, the spectra have been evaluated for several values of the rotational damping ratio ξ_φ (0.00; 0.05; 0.08; 0.10).
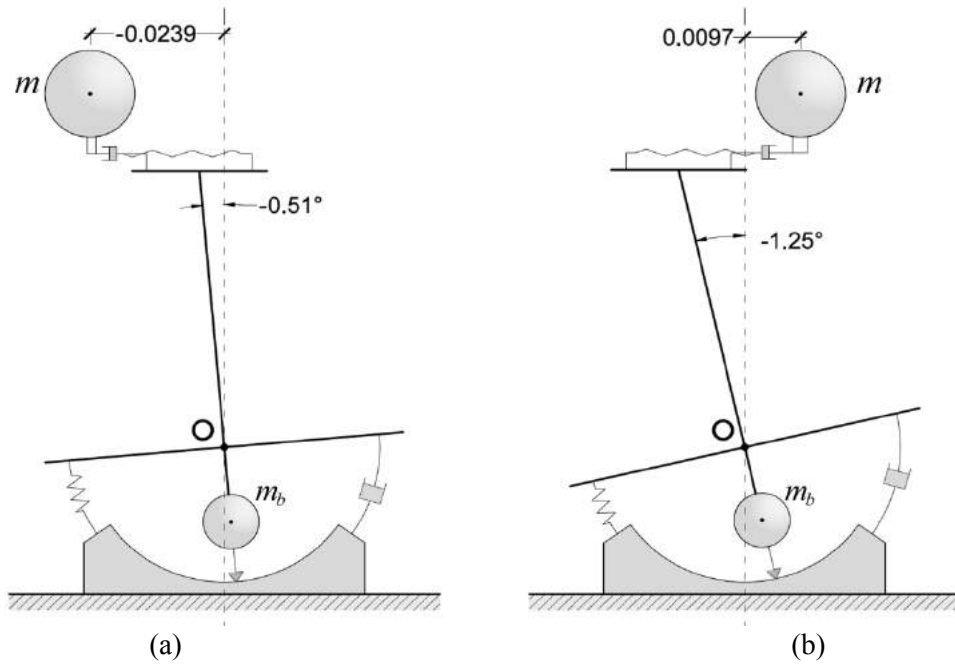
Figure 17 Modal shapes of vibration for $k_\varphi = 500$ kNm (measures in m): (a) fist mode Φ_1; (b) second mode Φ_2.

(a)   (b)
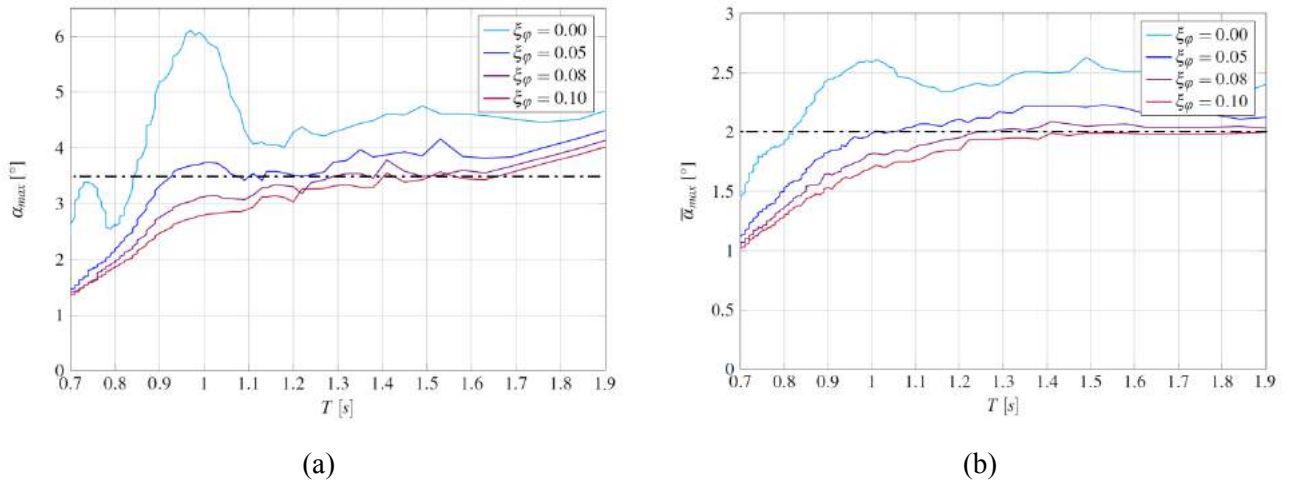
Figure 18 Displacement spectra for several values of the rotational damping ratio ξ_φ in the period range $T_1 = 0.7 - 1.9$s : absolute maximum rotation α_{max} (a) and mean of the maximum rotations $\overline{\alpha_{max}}$ (b).

As expected, rotations usually increase with the period, so highly isolated structures are also more demanding in terms of displacement capacity. Curves in **Figure 18**b appear concentric with a monotonic trend for lower periods and almost constant value for periods greater than 1.1 s. On the other hand, in **Figure 18**a rotations show a monotonic growth in the monitored range of periods with some fluctuations and a localized peak around the period $T = 1.0$ s probably due to resonance. In undamped conditions ($\xi_\varphi = 0$) these phenomena are emphasized; while it is definitely less relevant whether the damping ratio is greater than 0.05. This underlines the importance to put viscous elastic components into TROCKSISD. Acceptable rotation values are assumed to be the following:

$$\overline{\alpha}_{lim} = 2.0°$$

(41)

$$\alpha_{lim} = 3.5°$$

values that are well within the angular sliding stroke limit $\Delta\varphi = 5°$ (previous **Table 3**). The assumed limit rotations are displayed as dash-dotted lines in **Figure 18**. To meet these specific design objectives, the first period of the system could be selected as $T_1 = 1.4$ s, yielding the value of in-plane rotational stiffness of

$$k_\alpha = 200 \text{ kNm} \tag{42}$$

Moreover, the damping ratio that all the viscous elastic components have to score should be in the range of

$$\xi_\varphi = 0.08 - 0.10 \tag{43}$$

identified by purple and red lines in **Figure 18**.

5 Influence of friction on TROCKSISD performances

The role of friction has three purposes: to prevent the rocking mechanism at SLS (as investigated in Section 4), to dissipate energy at the ULS (discussed later in 6.3) and to limit the rotations. The parametric analysis performed in this Section has the aim of discussing the latter aspect. It appears clear that if friction is suppressed, the reactive role could be only played by the viscous elastic dampers. Therefore, to obtain a frictionless displacement spectrum that matches the original spectrum (where friction contribution is present), the damping capacity of these components is varied. For easy reference, the same geometric and mechanical parameters used in the previous section are employed. The friction coefficient is set on the $\mu_s = 0.18$ ($\mu_d = 0.09$) or alternatively on $\mu = \mu_s = \mu_d = 0.00$. In the first case, the rotational damping ratio is $\xi_\varphi = 0.08$, in the second it varies from $\xi_\varphi = 0.08$ to $\xi_\varphi = 0.25$.
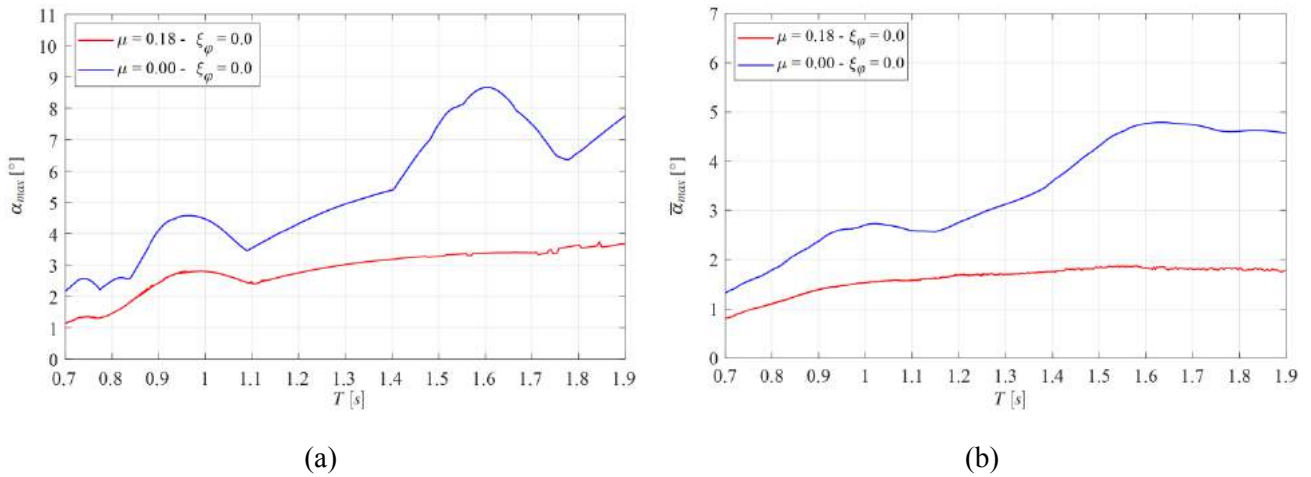
The displacement spectra of absolute maximum rotations α_{max} and mean value of the maximum rotations $\overline{\alpha_{max}}$ are reported in **Figure 19**. The curves exhibit some peaks due to resonance phenomena, which, as in previous cases (**Figure 18**), flatten when damping increases. With respect to the reference case-study curve ($\mu_s = 0.18$; $\xi_\varphi = 0.08$), both mean and absolute maximum rotations are magnified along the entire monitored spectrum if the friction is suppressed and dampers with same characteristics are adopted. Increasing the damping ratio, for values of periods smaller than 1.0 s the curves tend to approach the reference curve. For larger periods the curves diverge, and, while the reference curve tends to be constant, the frictionless curves are monotonically growing. To guarantee performances which are similar to those of a tribological device at least for lower periods, the viscous damping capacity should increase substantially, bringing to larger devices that may also impair the feasibility of the device.

(a)   (b)
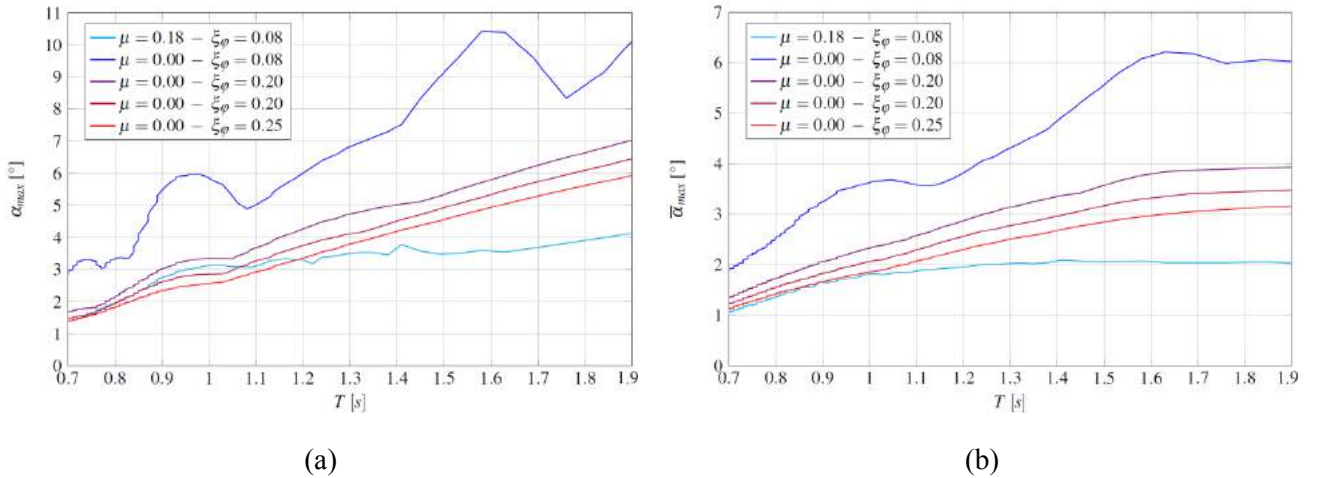
Figure 19 Displacement spectra for several values of the rotational damping ratio ξ_φ in the period range $T_1 = 0.7 - 1.9$ s with and without friction: absolute maximum rotation α_{max} (a) and mean of the maximum rotations $\overline{\alpha_{max}}$ (b).

For the case under examination, one would need of a value of damping ratio of about 20-25% to attain similar rotations reached for the case with friction (**Figure 19**). Consequently, the contribution of friction is fundamental both in the dynamic behavior to minimize the displacement and to increase the dissipative capacity, as well as in the economy of the device itself.

Displacement spectra are reported in **Figure 19** for the case of concomitant zerofriction ($\mu = \mu_s = \mu_d = 0.00$) and damping ratio ($\xi_\varphi = 0.00$). In addition, the case of the solely presence of friction ($\mu_s = 0.18$; $\mu_d = 0.09$) with null damping ratio ($\xi_\varphi = 0.00$) is investigated, to simulate the only presence of friction. In the first case, the rotations (both α_{max} and $\overline{\alpha_{max}}$) appear similar to the $\xi_\varphi = 0.08$ curves of **Figure 19**, confirming the main role of friction in the dynamics of TROCKSISD. On the other hand, the frictionless curves in **Figure 20**($\mu = 0.00, \xi_\varphi = 0.00$) show slightly smaller rotations with respect to the corresponding curves ($\mu = 0.00, \xi_\varphi = 0.08$) in **Figure 19**. However, a device without damping and friction would have no dissipative features. The curves with zero damping and friction diverse from zero ($\mu = 0.18, \xi_\varphi = 0.00$, **Figure 20**), have similar values of maximum rotations with respect to the case $\mu = 0.18, \xi_\varphi = 0.08$ (**Figure 19**), demonstrating that the amount of damping ratio 8% does not sensitively influence the maximum displacements.

(a)   (b)

Figure 20 Displacement spectra for null rotational damping ratio $\xi_\varphi = 0$ in the period range T_1 $= 0.7 - 1.9$ s with and without friction: absolute maximum rotation α_{max} (a) and mean of the maximum rotations $\overline{\alpha_{max}}$ (b).

## 6 Analysis results and discussion

The results of the dynamic analyses both at the SLS and at the ULS are collected in this section. The displacement time histories of both DOFs of the system under some significant natural accelerogram are reported. The results of the superstructure translational DOF at the ULS are compared with the response of a not-isolated Reference SDOF oscillator (ROS) with same geometric and dynamic properties.

6. 1 SLS dynamic response

For the present level of actions, friction substantially prevents the sliding of the base surfaces, namely the second DOF α of the system is blocked. **Figure 21** shows for the accelerograms S3 and S7 the displacement time-history of the two DOFs, x translational of the superstructure and α rotational of the jointed mechanism. **Table 4** summarizes the resulting maximum values. Concerning the first DOF, horizontal displacement is not larger than 11 mm, a value for which the superstructure is designed to behave elastically.

As evidenced by the second DOF plots, the dynamics is characterized by a prevailing stick phase; although some residual rotations still occur (**Figure 21**b). The reason is that the single accelerogram approximates the code spectrum, so some points inevitably generate larger actions. Rotations are indeed instantaneous and correspond to a specific acceleration local peak. However, despite its irreversibility, the magnitude of such

rotation is small and tolerable. The absolute maximum of the rotation occurs at S2 ($\alpha = 0.14°$), while the mean value of all data is $\overline{\alpha} = 0.07°$. The residual rotation is even smaller ($\alpha_r = 0.08°$; $\overline{\alpha}_r = 0.03°$) because the periodic nature of seismic action helps the system to re-center.
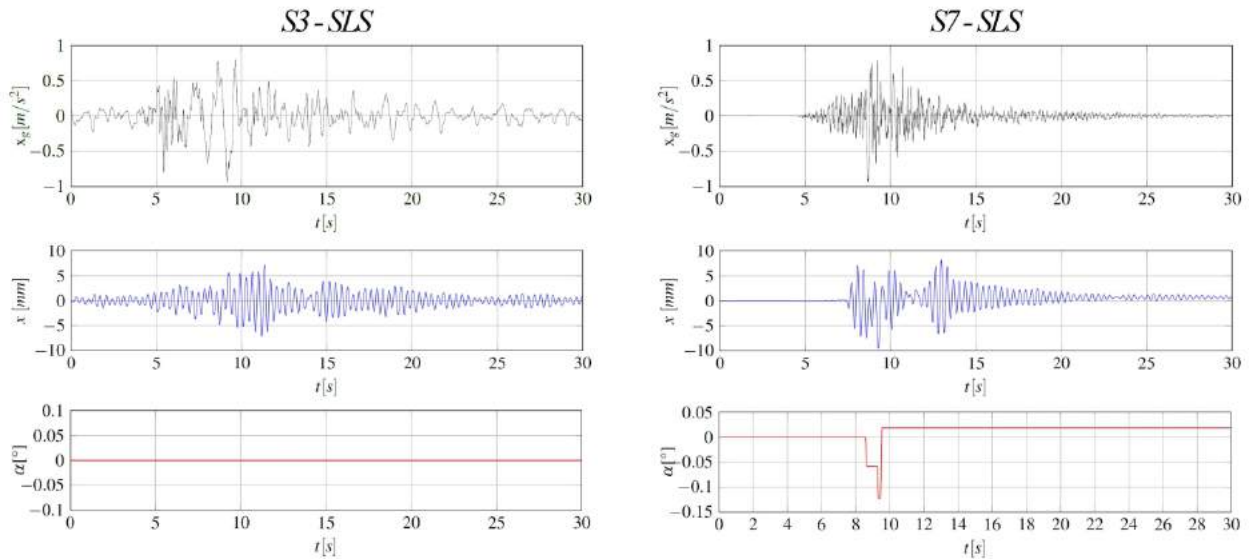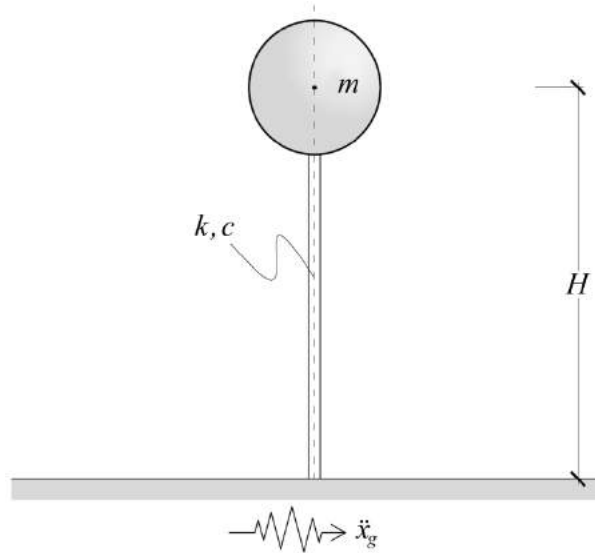

Figure 21 SLS dynamic response for S1 and S7 seismic records (in black the input record, in blue the horizontal displacement time-history, in red the rotation time-history).

Table 4 Main result of the dynamic analysis at the SLS: maximum values of horizontal displacement (x), rotation (α), and residual rotation at the end of motion α_r.

| Accelerogram	x (mm)	α (°)	α_r (°)
S1	9	0.06	0.06
S2	11	0.14	0.08
S3	7	0.00	0.00
S4	7	0.00	0.00
S5	9	0.09	0.02
S6	9	0.06	0.01
S7	9	0.12	0.02
Max	11	0.14	0.08
Mean	9	0.07	0.03

6.2 ULS dynamic response

The dynamic response can be evaluated at the ULS for the considered acceleration time-histories. For the sake of brevity, only the outcomes of some analyses are reported, e.g. for S4 and S7 seismic record, shown in **Figure 23**. To immediately compare the response of the isolated system, the results concerning the first DOF are plotted together with those of the reference SDOF oscillator (ROS) schematically reported in **Figure 22**.

Figure 22 Not-isolated reference SDOF oscillator (ROS).
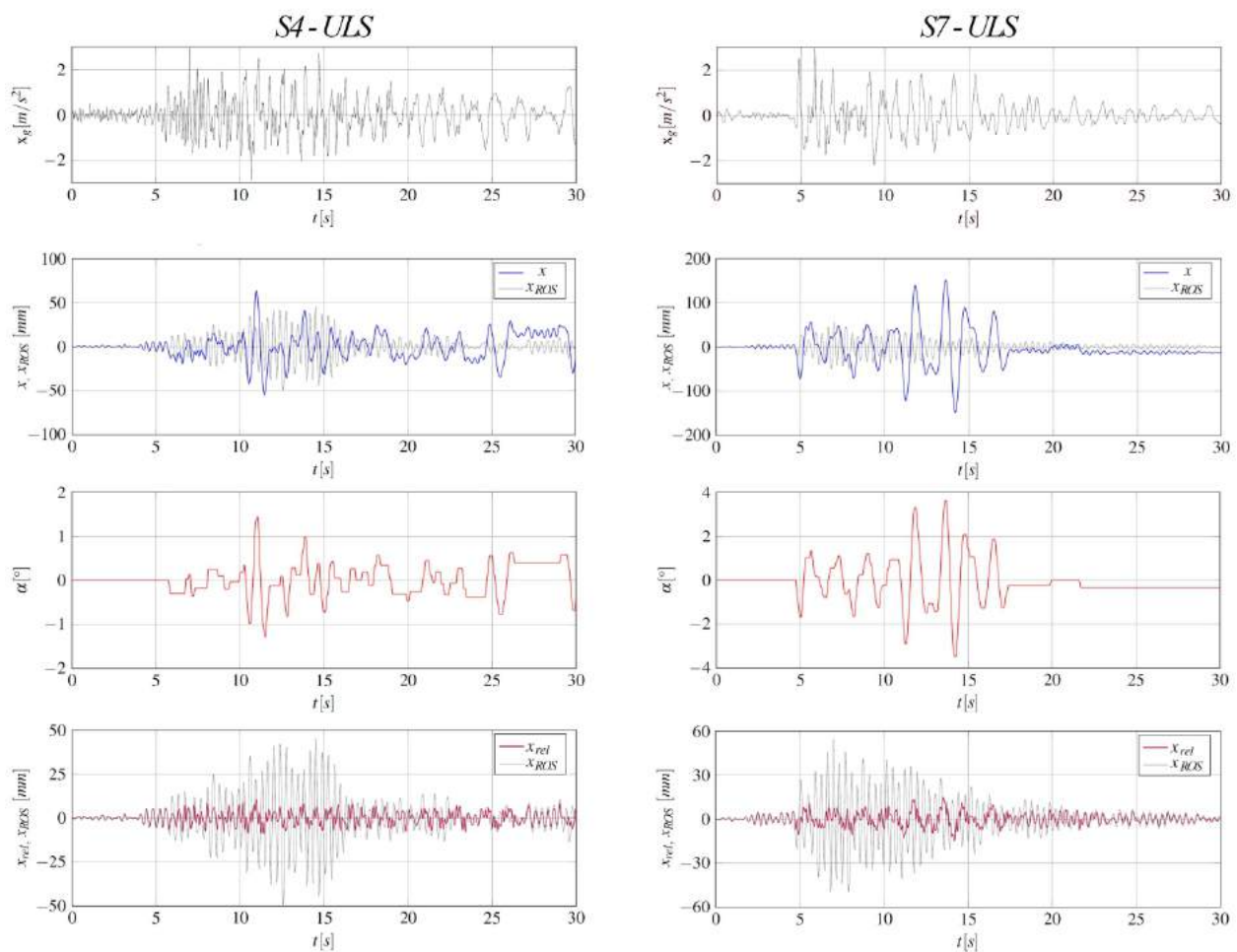
Figure 23 ULS dynamic response for S4 and S7 seismic inputs.

The first plot depicts the absolute horizontal displacement of both systems. As usual for isolated system, the superstructure equipped with TROCKSISD exhibits larger displacement than the ROS.

In the second plot the ROS curve is compared with the relative displacement of the superstructure mass x_{rel}, where the horizontal displacement due to rotations at the second DOF is deducted from the absolute value.

$$x_{rel} = x - h\alpha \tag{44}$$

The third plot that concerns the oscillations of the second rotational DOF shows the presence of a slip-stick motion with incipient motion phases included. Residual rotations occur at the end of each acceleration story. Their magnitudes, as in the SLS case, are relatively reduced, if compared with the maximum rotations.

The maximum values of displacement and rotation are reported in **Table 5**. In all cases, the rotation values are close to the limitation imposed in the design phase of 3.5° for the absolute maximum and 2.0° for the mean of maximum values. Concerning the translation of the first DOF, x_{max} values are meanly three times larger than these of x_{ROS} in terms of absolute values, or at least more than two times larger for the mean value (38 mm vs. 90 mm). This result is consistent with the strategy adopted of shifting the T_1 period towards higher values in order to gain from a reduced level of accelerations but paying with increased displacement. Nevertheless, it is interesting to observe that the relative displacement is about the 30% of the x_{ROS}. This outcome has two implications. First, the second DOF becomes successfully prevalent in the dynamics of the system, contrary to what might be thought from the mass participation in the modal analysis (**Figure 16**). Second, the superstructure equipped with TROCKSISD is less stressed than the ROS, since the inertial forces generated at the lumped mass m level, produce displacement x_{rel} and x_{ROS} respectively, which result smaller in the first case rather than in the second one.

Table 5 Main result of the dynamic analysis at the ULS: maximum values of horizontal displacement of ROS (x_{ROS}), absolute and relative horizontal displacement of the superstructure (x, x_{rel}) rotation (α), and residual rotation at the end of motion α_r.

| Accelerogram	x_{ROS} (mm)	x (mm)	$(x - x_{ROS})/x$	x_{rel} (mm)	$(x_{rel} - x_{ROS})/x_{rel}$	α (°)	α_r (°)
S1	36	31	-16%	9	-300%	0.68	0.08
S2	40	147	73%	15	-167%	3.51	0.19
S3	27	107	75%	12	-125%	2.53	0.20
S4	49	64	23%	11	-345%	1.43	-
S5	30	61	51%	11	-173%	1.34	0.19
S6	28	69	59%	10	-180%	1.55	0.21
S7	55	151	64%	15	-267%	3.56	0.33
Max	55	151	64%	15	-267%	3.56	0.33
Mean	38	90	58%	12	-217%	2.09	0.20

6.3 Energy dissipation

The energy dissipated can be regarded as the area delimited by the hysteresis loop M − α, where M is the loading bending moment and α is the rotational DOF. Particularly, M is the sum of three contributions (qualitatively represented in **Figure 24**):

- Elastic moment: $M_k = k_\varphi \, \alpha$
- Viscous moment: $M_c = c_\varphi \dot{\alpha}$
- Tribological moment: $M_\mu = M_{\mu, d}$
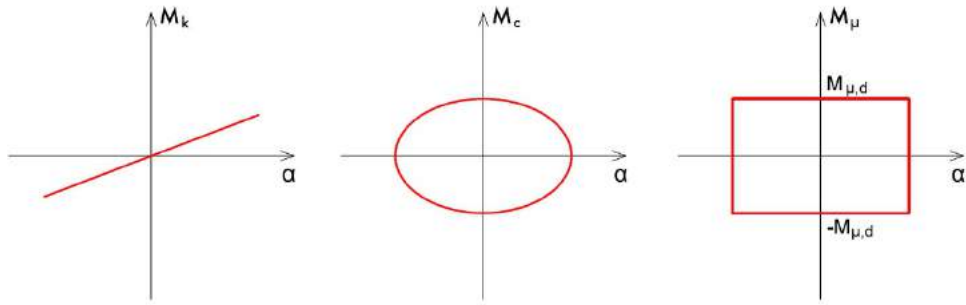
Figure 24 Qualitative hysteresis cycles of the three contributions of moment.

The hysteresis cycles obtained from the accelerograms S1 to S7 are represented in **Figure 25**. Despite the viscous capacity of dampers constitutes a non-negligible contribution in the dynamic motion of the system, from the energetic point of view the viscosity alters only slightly the area. Each cycle plot approximates a parallelogram, as the system is only elastic-frictionally isolated. To highlight this feature, in **Figure 26**, the curve with the only $M_k + M_\mu$ component is graphically compared with the total M curve for S4 and S7 accelerograms. Since no damage occurs during the motion of the system, the non-degrading behavior exhibited by curves in **Figure 26** appears accordingly reasonable.
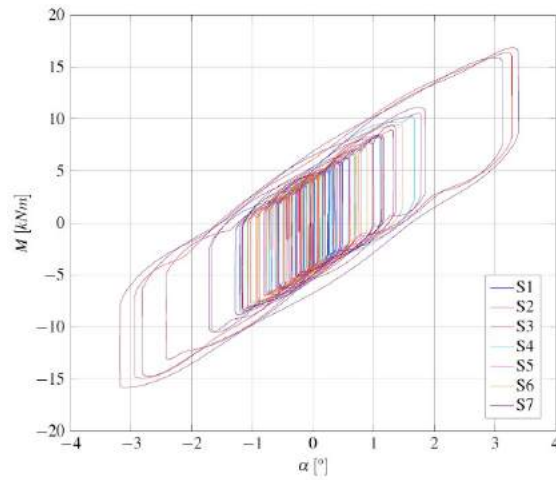
Figure 25 Hysteresis cycles M − α of all the accelerograms S1 to S7.
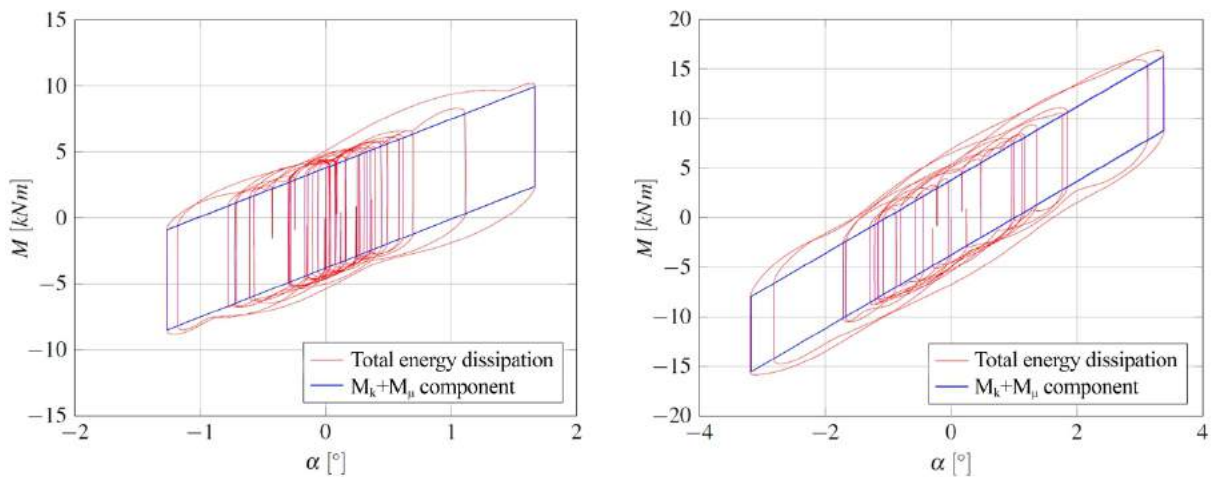
Figure 26 Hysteresis cycles M-α of selected accelerograms S4 and S7 in comparison with the $M_k + M_\mu$ component cycles.

7. Comparison between TROCKSISD and existing seismic isolation devices

Most of the traditional seismic isolation devices exhibit a purely translational dynamics (shear behavior), whereas TROCKSISD is based on a rocking motion that reduces the seismic demand of the superstructure. Even in the double concave surface sliders, the rotational dynamics eases the re-centering of the system once that the seismic input vanishes. However, unlike the inverted pendulum devices, TROCKSISD allows a relevant energy dissipation, due to (i) the presence of peripheral dampers and to (ii) the development of friction at the interface of the curved surfaces. Such a coupling of energy dissipation systems permits a reduction of the isolator size, aspect relevant in the preservation of artistic assets. Moreover, with respect to existing isolation devices, the polar symmetrical arrangement of the springs allows efficiently absorbing the vertical components of the dynamic motion.

In conclusion, the following phenomena occur with the use of TROCKSISD as seismic mitigation device:

- rocking mechanism not impeded, but allowed and *controlled*;
- automatic re-centering of the system thanks to the springs, with their circumferential and peripheral disposition to avoid undesired torsional motions and reducing the device size;
- relevant contribution of friction between the two spherical caps in the seismic energy dissipation;
- high energy dissipation level thanks to the rotational dynamics of the system;
- possibility of 3D rocking thanks to the polar symmetrical arrangement of the visco-elastic dampers.

8. Conclusions and future developments

The Tribological ROCKing Seismic ISolation Device (TROCKSISD) can provide seismic protection of slender structures and valuable objects such as artistic or historic assets (altars, statues, art objects, etc.). It is based on the development of friction at the interface of a jointed mechanism that allows smooth rocking of the superstructure in a frictional model. Energy dissipation as well as re-centering capability are provided by perimetral viscous elastic dampers and springs. The reactive static friction force can be designed to delimit two types of dynamic behavior of prevalent stick phase (at SLS) and of mixed slip-stick phase (at ULS), leading to a performance-based designed geometry and mechanics.

The behavior of a system equipped with such a device has been described by means of a simple 2DOFs analytical model, where the superstructure is essentially regarded as a simple oscillator with translational DOF. Based on the performances obtained from the simulations, the following concluding remarks can be drawn.

- A performance-based design approach is feasible, and it has been demonstrated with the case study presented, where the target rotations are met. At the SLS, rocking is substantially prevented, and, at the ULS, rotations occur within pre-fixed designed limits.
- The radius of the spherical cup defines the threshold of the incipient motion, which separate stick from slip motions. This design specification usually results in large radius so that the vertical and horizontal loading is easily transferred through the device without peaking the strength limit of the components. So generally, it can be asserted that the statics is not governing the problem as long as the radius is defined for the dynamics of the system.
- The amplitude of rotations at ULS are influenced by the mechanical characteristics of the dampers k_φ and ξ_φ, supposing constant the contribution of friction, whose tribological moment is derivable once designed the radius at the SLS.
- Friction constitutes a substantial contribution in impeding the rocking mechanism at SLS, reducing the rotations and dissipates energy at ULS. In terms of rotations, similar performances with a frictionless device can be achieved only with larger dampers, which are more expensive and, due to their size, may also impair the overall feasibility.
- At the ULS the absolute horizontal displacement of the lumped mass of the superstructure is larger if compared with the reference conventional ductile system, but, its relative displacement is rather

smaller, so the resulting stress on the superstructure is lowered. The jointed mechanism allows all the relative movements between the parts.

- Concerning isolation capabilities, two comments can be raised. First, the relative displacement of the superstructure at the ULS results smaller and close enough to the SLS displacement, despite the PGA, going from SLS to ULS, is usually doubling. The superstructure can indeed be designed to behave elastically at the isolated-ULS and so that can it will not report any damage. Second, the hysteresis plot shows that a large amount of energy can be dissipated through a non-degrading cyclic behavior, essentially due to friction. Friction developed for smooth contact of the sliding surfaces provides continuous energy dissipation and avoids undesired impacts (which in the case of stepping structures led to a degradation of the surfaces).

From the previous statements, it is clear that TROCKSISD follows DAD principles. Both the superstructure and the jointed device result undamaged after motion. The residual rotations at ULS shall be reversed once the excitation stops, guaranteeing immediate post-event serviceability. The device meets both the objectives of energy dissipation and control of displacements.

Further research is needed in the extension of the study to a more detailed model, e.g. the P-Delta effects generating by the rocking superstructure, and other design scenarios. The three-dimensional nature of loading and structural response, especially that related with the superstructure, would require a complete consideration of the spatial behavior. Moreover, experiments are going to be performed by the authors to confirm the analytical results.

References

[1]   J. B. Mander and C.-T. Cheng, "Seismic resistance of bridge piers based on damage avoidance design," 1997.

[2]   M. Pollino, "Seismic design for enhanced building performance using rocking steel braced frames," *Eng. Struct.*, 2015.

[3]   G. W. Housner, "The behavior of inverted pendulum structures during earthquakes," *Bull. Seismol. Soc. Am.*, vol. 53, no. 2, pp. 403–417, 1963.

[4]   J. W. Meek, "Dynamic response of tipping core buildings," *Earthq. Eng. Struct. Dyn.*, 1978.

[5]   M. Aslam, W. G. Godden, and D. T. Scalise, "Earthquake Rocking Response of Rigid Bodies," *J. Struct. Div.*, vol. 106, no. 2, pp. 377–392, 1980.

[6]   L. Collini, R. Garziera, K. Riabova, M. Munitsyna, and A. Tasora, "Oscillations Control of Rocking-Block-Type Buildings by the Addition of a Tuned Pendulum," *Shock Vib.*, pp. 1–11, 2016.

[7]   C. Casapulla; L. U. Argiento, "In-plane frictional resistances in dry block masonry walls and rocking-sliding failure modes revisited and experimentally validated," *Compos. Part B Eng.*, vol. 132, pp. 197–213, 2018.

[8]   P. B. Casapulla, C., Giresini, L., Sassu, M., Lourenço, "Rocking and kinematic approaches of masonry walls: state of the art and recent developments," *Buildings*, 2017.

[9]   C. Casapulla and A. Maione, "Formulating the torsion strength of dry-stacked stone blocks by comparing convex and concave contact formulations and experimental results," *Indian J. Sci. Technol.*, vol. 9, no. 46, p. 107346, 2016.

[10] T. Hanazato, T. Nagai, K. Yanagisawa, K. Hidaka, I. Sakamoto, and M. Watabe, "Greek temple and timber Pagoda in Japan-comparison of the aseismic structural performances," *WIT Trans. Built Environ.*, vol. 42, 1970.

[11] J. L. Beck and R. I. Skinner, "Seismic Response of a Reinforced Concrete Bridge Pier Designed to Step," *Earthq. Eng. Struct. Dyn.*, 1974.

[12] R. D. Sharpe and R. I. Skinner, "The seismic design of an industrial chimney with rocking base," *Bull. New Zeal. Natl. Soc. Earthq. Eng.*, vol. 16, no. 2, pp. 98–106, 1983.

[13] M. J. N. Priestley, S. (Sri) Sritharan, J. R. Conley, and S. Stefano Pampanin, "Preliminary Results and Conclusions From the PRESSS Five-Story Precast Concrete Test Building," *PCI J.*, 1999.

[14] L. Sorrentino, D. D'Ayala, G. de Felice, M. C. Griffith, S. Lagomarsino, and G. Magenes, "Review of Out-of-Plane Seismic Assessment Techniques Applied To Existing Masonry Buildings," *Int. J. Archit. Herit.*, vol. 11, no. 1, pp. 2–21, 2017.

[15] C. Casapulla and A. Maione, "Critical Response of Free-Standing Rocking Blocks to the Intense Phase of an Earthquake," *Int. Rev. Civ. Eng.*, vol. 8, no. 1, 2017.

[16] L. Giresini, "Design strategy for the rocking stability of horizontally restrained masonry walls," in *COMPDYN 2017 6th ECCOMAS Thematic Conference on Computational Methods in Structural Dynamics and Earthquake Engineering*, 2017.

[17] L. Giresini, M. Fragiacomo, and P. B. Lourenço, "Comparison between rocking analysis and kinematic analysis for the dynamic out-of-plane behavior of masonry walls," *Earthq. Eng. Struct. Dyn.*, vol. 44, no. 13, pp. 2359–2376, 2015.

[18] L. Giresini and M. Sassu, "Horizontally restrained rocking blocks: evaluation of the role of boundary conditions with static and dynamic approaches," *Bull. Earthq. Eng.*, vol. 15, no. 1, pp. 385–410, 2017.

[19] L. Giresini, M. Fragiacomo, and M. Sassu, "Rocking analysis of masonry walls interacting with roofs," *Eng. Struct.*, vol. 116, pp. 107–120, Jun. 2016.

[20] N. Makris and M. F. Vassiliou, "Dynamics of the Rocking Frame with Vertical Restrainers," *J. Struct. Eng.*, vol. 141, no. 10, 2015.

[21] G. Oliveto, I. Cali??, and A. Greco, "Large displacement behaviour of a structural model with foundation uplift under impulsive and earthquake excitations," *Earthq. Eng. Struct. Dyn.*, 2003.

[22] S. Acikgoz and M. J. Dejong, "The interaction of elasticity and rocking in flexible structures allowed to uplift," *Earthq. Eng. Struct. Dyn.*, 2012.

[23] I. Caliò and A. Greco, "Large displacement behavior of a rocking flexible structure under harmonic excitation," *JVC/Journal Vib. Control*, 2016.

[24] K. Muto, H. Umemura, and Y. Sonobe, "Study of the overturning vibrations of slender structures," in *Proceedings of the 2nd World Conference on Earthquake Engineering. Tokyo, Japan*, 1960, vol. 2, pp. 1239–1261.

[25] I. N. Psycharis and P. C. Jenning, "Rocking of slender rigid bodies allowed to uplift," *Earthq. Eng. Struct. Dyn.*, vol. 11, pp. 57–76, 1983.

[26] S. Baggio, L. Berto, T. Favaretto, A. Saetta, and R. Vitaliani, "Seismic isolation technique of marble sculptures at the Accademia Gallery in Florence: numerical calibration and simulation modelling," *Bull. Earthq. Eng.*, vol. 13, no. 9, pp. 2719–2744, 2015.

[27] J. W. Meek, "Effects of Foundation Tipping on Dynamic Response," *Journal of Structural Division.* 1975.

[28] A. A. Huckelbridge and R. W. Clough, "Seismic response of uplifting building frame," *J. Struct. Div.*, vol. 104, no. 8, pp. 1211–1229, 1978.

[29] R. Ceravolo, M. L. Pecorelli, and L. Z. Fragonara, "Semi-active control of the rocking motion of monolithic art objects," *J. Sound Vib.*, vol. 374, pp. 1–16, 2016.

[30] S. Baggio, L. Berto, I. Rocca, and A. Saetta, "Vulnerability assessment and seismic mitigation intervention for artistic assets: from theory to practice," *Eng. Struct.*, vol. 167, pp. 272–286, 2018.

[31] M. Erdik, E. Durukal, and N. Erturk, "Seismic risk mitigation in Istanbul museums," in *Advances in the protection of museum collections from earthquake damage: papers from a symposium held at the J. Paul Getty Museum at the Getty Villa on*, 2006, pp. 95–105.

[32] M. Lowry, D. Armendariz, B. J. Farra, and J. Podany, "Seismic mount making: a review of the protection of objects in the J. Paul Getty Museum from earthquake damage," in *Advances in the protection of museum collections from earthquake damage, symposium held at the J. Paul Getty museum at the Getty Villa, Malibu, United States*, 2006.

[33] D. Sonda, A. Cigada, E. Zappa, and M. Cossu, "SEISMIC AND VIBRATION PROTECTION OF THE STATUE" PIETA'RONDANINI" BY MICHELANGELO," in *16th World Conference on Earthquakes, 16 WCEE 2017*, 2017.

[34] G. De Canio, S. Bonomi, and A. Cannistrà, "Anti-Seismic Marble Basements for High Vulnerable Statues in Italy: Bronzes of Riace, Annunciazione by Francesco Mochi San Michele Arcangelo by Matteo di Ugolino," *Knowledge, Diagnostics Preserv. Cult. Herit.*, no. EAI Special-NATURAL RISKS AND PROTECTION, pp. 56–62, 2012.

[35] K. Worden and G. R. Tomlinson, "NONLINEARITY IN STRUCTURAL DYNAMICS. Detection, Identification and Modelling," *Physics (College. Park. Md).*, p. 670, 2001.

[36] R. W. Clough and J. Penzien, *Dynamics of Structures*. 2013.

[37] I. Iervolino, C. Galasso, and E. Cosenza, "REXEL: Computer aided record selection for code-based seismic structural analysis," *Bull. Earthq. Eng.*, 2010.

[38] K. Lin, H. Liu, C. Wei, and Q. Huang, "Effects of shear rate on cyclic behavior of dry stack masonry joint," *Constr. Build. Mater.*, vol. 157, pp. 809–817, 2017.